ISSN: 0976-9102 (ONLINE)
DOI: 10.21917/ijivp.2026.0549

ENHANCED BIAS MITIGATION AND SCRUPULOUS 3D RECONSTRUCTION IN 2D BRAIN MR IMAGING: A MULTI-LAYERED APPROACH

A. Farzana[1] and M. Mohamed Sathik[2]
[1]*Department of Computer Applications, Sadakathullah Appa College, India*
[2]*Department of Computer Science, Francis Xavier Engineering College, India*

Abstract

Computer Assisted Diagnosing (CAD) plays a vital role in healthcare education, surgical training and treatment planning. The backbone of CAD is medical images. The 2D medical images will lack the ability to interpret the information. 3D model construction helps to abolish the hurdle. The 2D medical images can be corrupted by Intensity In-Homogeneity (IIH) or bias. Lesser Intensity In-Homogeneity is hardly noticeable but can cause organ loss while reconstructing a 3D model. The purpose of this research work is to present a novel multi-layered approach that accurately removes the barely perceptible bias, segments the image organ and reconstructs a 3D model from the bias-influenced brain MR images. A Benchmark data set with different bias spectra is used for this research. The formulated 3D model is precise in its illustration without any organ loss.

Keywords:

Brain MRI, Bias, Intensity In-Homogeneity, Segmentation, 3D Reconstruction

1. INTRODUCTION

Technology plays a significant part in the advancement of the clinical field. The principal objective of the CAD framework is to recognize anomalous signs at the most punctual time that a human expert struggles to discover. The doctors and radiologists find it challenging to decipher the 2D medical images. 3D models are utilized, which serve to picture the organs accurately, help practitioners to learn complex life structures, assist radiologists and specialists to think about the severances of the malady, and help them in treatment arranging. Medical image qualities are often affected by artifacts, noise, blurring, contrast sensitivity, and bias. Bias is influenced by both patients and machines. Impacted by patient movement, anatomical structures, alignment of radio frequency coils, and aged MRI machines build a low-frequency shading effect over the developed medical images [1-10], which is also termed by shading, Intensity In-Homogeneity (IIH) and Intensity Non-Uniformity (INU).

Bias correction techniques are branched under two categories: they are prospective and retrospective. The previous strategy attempted to dispose of IIH at the time of image acquisition, and it is purely machine-dependent [11-14], whereas the latter method is based on the image and signal processing techniques such as intensity-based, domain-based, spatial filtering, surface fitting, and statistical methods-based bias estimation and correction strategies [15-16]. More than forty percent bias is only noticeable by the beholder. This is because human eyes struggle to differentiate between fifty different shades of grey, while machines can easily distinguish them. Lesser bias is invisible and still can produce erroneous outcomes in segmentation and 3D model construction. There are several INU correction and INU correction-based segmentation techniques proposed to date. The automatic bias correction strategy is proposed for liver MR images based on local, global, and spatial intensity information. Where the background noise elimination is performed as a pre-processing step and the region-growing algorithm is implemented for segmentation [17]. A novel fuzzy clustering technique is proposed by incorporating contextual objective and Gaussian membership methods in the process of simultaneous bias reduction and segmentation [18]. A different approach is recommended for INU correction in brain MR images [19]. The primary intention is to fuse spatial intensity data with a modified membership matrix function of traditional fuzzy c-means clustering. However, the run time is higher than the state-of-the-art techniques. Several bias estimations, corrections, and segmentation strategies have been recommended using fuzzy clustering, but this technique is highly sensitive to noise, and algorithm performance is solely based upon the initialization of cluster seed points [20-25]. The Coherent Local Intensity Clustering Technique is recommended for Intensity Non-Uniformity correction. The correction strategy builds over the regional intensity information in the brain MR Images. At the point when images are ruined by extreme Intensity In-Homogeneity this procedure neglects to characterize the edge pixels, and the performance of this algorithm is restricted with respect to noise and bias spectrum [26]. The modified Possibilistic Fuzzy C Means technique is suggested for bias correction [27]. It incorporates local and global intensity information to expel the bias. But this technique mistakenly removes the lower intensity information present in the original image.

After bias removal, segmentation techniques were adopted to partition the image components. Several segmentation techniques are proposed; they are edge-based, region-based, threshold-based, neural network-based, and clustering-based segmentation algorithms. A framework for energy minimization was built by combining Markov Random Field segmentation [28]. The initial estimation of this framework is weighed using the clustering method. The Multiplicative Intrinsic Component Optimization (MICO) technique is proposed for bias estimation, correction, and segmentation of brain MR images, where the initial image deteriorated into two multiplicative components, such as true image and bias field [29]. The bias-corrected fuzzy C-means algorithm is proposed by modifying the fuzzy clustering algorithm. The piecewise homogeneous labeling property is utilized to abolish the bias present in MRI data [30]. Gaussian distribution function and sliding window protocol are used for simultaneous bias correction and segmentation [31]. Li et al. proposed a level-set approach for segmentation and bias correction, but this technique fails to differentiate the intensity of variant pixels in image components [32]. Wang et al. recommend a method by incorporating gradient operation to fix the Intensity In-Homogeneity but it enforces the smoothness by reducing the gradient operation [33]. The Linear Intrinsic Component (LIC)

Model is proposed for simultaneous Intensity In-Homogeneity correction and segmentation, where the bias field is assumed to be linear, additive, and multiplicative components, which are derived to remove bias from uncomplicated noisy images. A novel Mumford-Shah model was proposed, which uses a regularization term to model the bias and two-stage segmentation using simple thresholding to segment the images [34]. The process of correction for bias field and segmentation is a very important pre-processing stage in magnetic resonance (MR) image analysis due to the presence of intensity inhomogeneity which can deteriorate image quality. In order to tackle this problem, some scientists have developed a model for the joint bias field correction and segmentation task. The model simultaneously corrects the bias field and performs image segmentation based on the assumption that the bias field is a combination of linear, additive and multiplicative models. Mathematical modeling has been used to eliminate bias from noisy and inhomogeneous images. Later, a new Mumford-Shah method was designed. A novel solution is recommended by adding an expectation maximization algorithm to expel the bias, but it requires manual intervention; if the initial assumption is incorrect, the algorithm fails to offer the expected outcome [35]. The Fuzzy C Means algorithm is modified to overcome the bias, but it is sensitive to noise, and its computational cost is high [36]. Li et al. proposed an algorithm for bias correction using the level set method, but it provides an unauthenticated outcome when the foreground and background of image intensity are merely the same [37]. An enhancement-based bias correction algorithm was proposed, which uses dynamic stochastic resonance for bias normalization; the limitation of this algorithm was that the execution time was higher [38]. An edge detection algorithm combined with a Bayesian-based level set technique is used to segment the brain MR images collected from the BRATS and Brain Web repositories. The selection of appropriate segmentation techniques relies upon the application. Moreover, a bias correction approach based on enhancement has been proposed using Dynamic Stochastic Resonance in order to correct intensity inconsistencies and enhance the image contrast. However, despite providing satisfying results, the algorithm exhibits increased computation time and complexity issues. Additionally, algorithms for edge detection, along with Bayesian level set segmentation have been implemented on brain MRI data extracted from BRATS and BrainWeb database, thus improving tumor localization and anatomical segmentation. In general, the performance of a bias correction or segmentation approach is strongly determined by the image properties and noise present in the data, as well as computational limitations and applications in medical imaging.

Segmented image slices are utilized for 3D reconstruction. Several surface- and volume-based 3D reconstruction techniques have been proposed, such as marching cubes, ray casting, maximum intensity projection, and texture mapping [39] [40]. The segmented images are used by ray casting and modified marching cubes algorithms to construct surface- and volume-based 3D models [41]. Several software packages are used to provide 3D views of medical images, such as 3D Doctor, OsiriX, MIPAV, ITK Tool Kit, Mimics, and BrainSuite [42]. The fatal MRI data is 3D reconstructed by removing the artifacts that arise during the image capturing and registration procedure. The slice-to-volume registration and super-resolution are used to accomplish the goal. The absolute intensity is used rather than spatial information. To obtain accurate intensity, N4 bias correction is implemented as a pre-processing step [43]. To reduce the processing time of image processing techniques, the parallel programming concept is included in graphical processing units, where the 3D model is constructed six times faster by using Fuzzy C Means segmentation and the marching cube algorithm [44]. A framework was built to analyze and visualize the brain MRI; the threshold-based segmentation technique was used to segregate the brain tumor. Tumors are classified into benign or malignant types by using feature extraction and support vector machine techniques. Then it is visualized in 3D using the marching cubes algorithm [45]. The traditional marching cubes algorithm is refitted by adding histogram pyramids to construct a smooth 3D model in less computation time. Image coordinates and intensities are used in constructing histogram pyramids [46]. However, none of the techniques discusses the impact of non-perceptible bias on 3D model construction. The major assumption is that lesser bias, which is unnoticeable, can't affect computer-aided diagnosing. This paper is an extension of the author's previous works [47], in which four state-of-the-art bias correction algorithms were scrutinized: LEMS, MICO, and N3. The result states that the N3 algorithm performs well in removing the lesser bias in brain MR images [47][48]. Indeed, the application of N3 can yield excellent results since the algorithm efficiently corrects the smooth variations of intensity levels. However, although possessing a number of valuable features, N3 is limited by its dependency on foreground extraction precision. As a result, any mistakes in background segmentation may negatively impact the effectiveness of bias removal and lead to some distortion and decrease in the precision of reconstruction. Moreover, the bias removal performed by N3 may yield certain irregularities within the resulting image that could further affect other image processing tasks, including tissue classification and segmentation and creation of a three-dimensional brain model. In order to address these weaknesses, the current research suggests an advanced and efficient algorithm for performing bias correction with a focus on precise foreground extraction and effective intensity normalization. The algorithm developed in this research will also provide means to create a three-dimensional brain model required for diagnosis, surgery planning, and medical visualization. However, the N3 algorithm's efficiency will be limited because of imprecise foreground extraction. This paper nominates an efficient technique that discards the lesser bias, constructs the accurate 3D model, and deliberately examines the shortcomings caused by the lesser bias. Additionally, a thorough analysis of the problems that result from residual bias fields is conducted, analyzing their effect on the quality of images, accuracy of segmentation, and 3D reconstructions. The objective of this analysis is to develop a reliable technique for bias field correction to improve both performance and quality of MR imaging applications on the brain.

The succeeding paper is formulated as follows: Section 2 incorporates the technical background related to the bias field model, section 3 portrays the detailed description of the proposed algorithm, section 4 contains the result and discussion, and section 5 summarizes the outcome.

2. BIAS FIELD MODEL

The fundamental logic behind bias correction is reclaiming the primary image intensities. The bias field can be represented as a lesser frequency, gently fluctuating multiplicative or additive function. The bias artefact in image signals can be modelled as,

$$F(x,y) = I(x,y)\, B(x,y) + N(x.y) \quad (1)$$

F(x,y) is bias influenced image, I(x,y) is a true image, B(x,y) is an added bias, it is smoothly varying multiplicative field. The noise term N(x,y) is Gaussian or zero mean additive noise. In bias correction strategies, the noise term is typically overlooked. If bias field is known, then the initial image signals can be easily retrieved.

$$I(x,y) = F(x,y) / B(x,y) \quad (2)$$

By performing logarithmic transformation on the equation (1), the model is transfigured into additive as follows,

$$F_{log}(x,y) = I_{log}(x,y) + B_{log}(x,y) \quad (3)$$

$F_{\log}(x,y)$, $I_{\log}(x,y)$, $B_{\log}(x,y)$ are logarithmic transformation of $F(x,y)$, $I(x,y)$ and $B(x,y)$.

3. PROPOSED METHOD

The recommended strategy emphasizes exact bias correction in order to create an accurate 3D model. The process flow of the proposed algorithm is depicted in Fig.1.

3.1 INPUT IMAGE

The brain MR Images with lower bias spectra with the characteristics of hardly noticeable and having no noise are given as an input.

3.2 MULTI LAYERED BIAS MITIGATION

Bias correction is a crucial pre-processing step that must be completed prior to segmentation and 3D reconstruction. The bias mitigation process comprises the following phases: Gradient Calculation, Texture Refinement, Logarithmic Transformation, ROI Extraction and Kernel Construction. The bias-corrected images are subjected to the segmentation and 3D reconstruction procedures.

3.3 GRADIENT CALCULATION

Bias field is considered as a smooth shading artifact that is superimposed on the original image. Intensity Non-Uniformity causes the image intensities to appear darker on one side and brighter on the opposite side. The gradient operation is used to examine the directional modulation of pixel intensities in the image. The gradient magnitude and gradient direction indicate the rate of intensity change at a given point and the direction (angle) where the intensity changes most rapidly. Intensity variations are evaluated along the x-axis, y-axis, and diagonal (xy) axis for each pixel at position (x,y).

3.3.1 Gradient Calculation in X direction:

The x-gradient measures the rate of intensity change in the horizontal (left-to-right) direction of the image. The gradient in the x-direction at pixel (x,y), is computed by comparing the intensity of the pixel at (x+1,y) with the pixel at (x,y).

$$\nabla x\, I(x,y) = I(x+1,y) - I(x,y) \quad (4)$$

where, $I(x,y)$ is the intensity of the image at the pixel location (x,y). $I(x+1,y)$ is the intensity of the pixel to the right of (x,y). This calculation gives you the difference in intensity between adjacent pixels horizontally.

3.3.2 Gradient Calculation in Y direction:

The y-gradient measures the rate of intensity change in the vertical (top-to-bottom) direction. The gradient in the y-direction at pixel (x,y), is computed by comparing the intensity of the pixel at (x,y+1) with the pixel at (x,y).

$$\nabla_y I(x,y) = I(x,y+1) - I(x,y) \quad (5)$$

where, $I(x,y)$ is the intensity of the image at the pixel location (x,y). $I(x,y+1)$ is the intensity of the pixel directly below (x,y). This calculation gives you the difference in intensity between adjacent pixels vertically.

3.3.3 Gradient in the XY-direction (Diagonal Gradient)

The XY-gradient (diagonal gradient) computes the rate of intensity change along the diagonal direction of the image, combining both horizontal (X) and vertical (Y) changes.

$$\nabla_{xy} I(x,y) = \sqrt{\left[I(x+1,y+1) - I(x,y)\right]^2 + \left[I(x+1,y) - I(x,y+1)\right]^2} \quad (6)$$

where, $I(x+1,y+1)$ is the intensity of the pixel diagonally down-right from (x,y). $I(x+1, y)$ is the intensity of the pixel to the right of (x,y). $I(x, y+1)$ is the intensity of the pixel directly below (x,y). These gradients enable us to capture intensity variations in several directions, which is critical for understanding and adjusting for bias fields.

3.4 TEXTURE REFINEMENT:

Smoothing operation is performed to abolish the estimated bias by implementing Gaussian kernel. This texture refinement operation is carried over in the entire image.

3.5 LOGARITHMIC TRANSFORMATION

Logarithmic transformation is applied to emphasize the lower intensity pixels, especially in regions with low contrast. Image texture features are enhanced using anisotropic filtering. The anisotropic diffusion process can be described by the partial differential equation,

$$\frac{\partial T}{\partial t} = \mathrm{div}\left(d(x,y)\nabla I\right) \quad (7)$$

where $\partial T/\partial t$ denotes the intensity variation over time. div stands for the divergence. ∇I is the gradient of the image intensity. $d(x,y)$ is the diffusion coefficient, which varies based on the gradient magnitude to control smoothing.

$$d(x,y) = \exp\left(-\frac{|\nabla I(x,y)|^2}{k^2}\right) \quad (8)$$

where, $|\nabla I(x,y)|$ is magnitude of the gradient at pixel (x,y). k is a threshold parameter which controls the sensitivity of gradient. Larger values of k permit more diffusions which helps to preserve edges. Anisotropic filtering is intended to upgrade the sharpness of textures by preserving the original image information.

3.6 ROI EXTRACTION

The edge pixels in the image are highly deteriorated by bias, accurate foreground extraction is a difficult yet fundamental step in restoring the image intensities. The input images are of grey scale. A simple thresholding approach is employed to isolate the foreground, and the resultant foreground is in binary form.

3.7 KERNEL CONSTRUCTION

The extracted foreground region may lack precision due to bias. An infinite number of nuclear particles and artifacts will be found around the retrieved foreground. A kernel will be built by revising the foreground, which incorporates the succeeding operations: (i) The morphological operator is utilized to suffuse the discontinuities present in the extracted foreground. (ii) Air voxel present in brain, portrayed as darker intensities in the MRI, which is neglected in foreground extraction, inclusion of image organs is essential in constructing mask. (iii) The microscopic artifacts near the extracted foreground should be neglected using the morphological operators. (iv) Labels are assigned by incorporating region property area and the binary kernel with accurate foreground was developed.

3.8 BIAS CORRECTION

The output of the logarithmically transformed image will be augmented with a constructed kernel to obtain the bias-corrected image.

3.9 DISTANCE REGULARIZED LEVEL SET EVALUATION (DRLSE) BASED SEGMENTATION

This is an upgradation of classical level set algorithm. Energy, Regularization property and potential term are used in constructing the DRLSE Technique [49]. The DRLSE approach is an improvement of the conventional level set approach in that it resolves the difficulties of numerical instability and re-initialization which occur in contour evolution. Contour starts at the zero level and expanded towards the desired location. The external energy term helps in moving the contour to expected desired position. Let φ, Ω be the level set function and the domain. Then energy function $E(\phi)$ is defined by,

$$E(\phi) = \mu R_P(\phi) + E_{\text{ext}}(\phi) \tag{9}$$

where μ is a constant, $R_P(\phi)$ is the distance regularization term, $E_{ext}(\varphi)$ is the external energy over the curve and P is the potential function [$P(0 :\infty)$ -> R].

$$R_P(\phi) = \int_\Omega P(|\nabla\phi|)\,dx \tag{10}$$

Distance regularization term ($R_P(\phi)$) along with potential function (P) manipulates the level set function by computing diffusion strategies. Due to the fact that regularization makes sure that the level set function has nearly constant gradient, any abnormalities such as sharp changes or flat areas are eliminated. As a consequence of the above process, the stability of the contour evolution is ensured and no re-initialization will be required. Double well potential function P is defined by,

$$P_2(s) = \begin{cases} \frac{1}{(2\pi)^2}\left(1-\cos(2\pi s)\right), & s \le 1 \\ \frac{1}{2}(s-1)^2, & s > 1 \end{cases} \tag{11}$$

S is a minimal point. To attain high smoothing effect, the minimal point will have customized to zero and one. By analysing with traditional level set algorithm, the DRLSE algorithm cut down the computational period by avoiding the re initialization process.

If the magnitude of the gradient moves away from those desired values, the forces produced by the potential will act on the level set function to return it to its desirable shape. This process allows for the evolution of the contour while still retaining the necessary edge information.

With the double-well potential, both forward and backward diffusions are accomplished simultaneously. While forward diffusion acts on noisy parts of the level set function, backward diffusion enhances the contour close to object edges. As a result, the level set will be able to evolve correctly to reach the desired target edges.

Different from the conventional level set formulation, the distance regularization technique makes use of an extra potential term which eliminates the need for reinitialization of the signed distance property. This makes the algorithm more stable and thus converges much faster, improving the results of brain MRI image segmentation and other applications such as three-dimensional reconstruction.

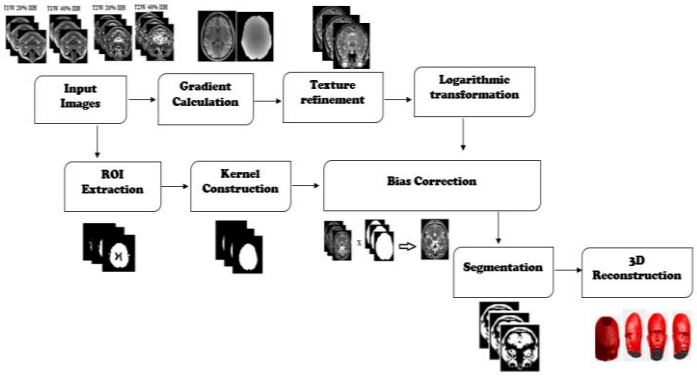

Fig.1. Process flow of the proposed algorithm.

3.10 MARCHING CUBES ALGORITHM

The algorithm was proposed by Lorensen and cline [50]. Marching cube algorithm is adopted to provide 3D view from 2D slices. Marching cube algorithm builds surface-based 3D reconstruction which uses the divide and conquer technique. Cubes are built between two adjacent image slices. Each cube incorporated 8 vertices, which leads to 256 intersecting points. These intersecting points are narrow down into 15 patterns. These patterns represent the pixels' state and location. The 3D model is formulated by the use of 15 intersecting patterns.

4. RESULT AND DISCUSSION

A collection of benchmark datasets gathered from the BrainWeb repository [51] are used to test our suggested approach.

The dataset's characteristics include T1 and T2 brain MR image types with one millimeter thickness, zero percent noise, and zero, twenty, and forty percent added Intensity Non-Uniformity Fig.2 displays the many sorts of input images. Although the input images appear to be of high definition, bias affects them. Bias is barely noticeable since it is less prevalent. One hundred and eighty-one slices of brain MR images make up each category. Three cutting-edge bias correction algorithms LEMS [52][53], MICO [54], and N3 [55] are compared to our recommended approach. All datasets, tools, and coding employed are all openly accessible.

The quality of bias correction is measured using the quantitative metrics Coefficient of Variation (CV) and the Coefficient of Joint Variation (CJV). Cerebrospinal fluid, a much smaller region, White Matter (WM), and Grey Matter (GM) are the three primary tissues visible in the brain imaging. For this reason, CV and CJV are calculated using only grey and white matter.

$$CV(x) = \frac{\sigma(x)}{\mu(x)} \tag{12}$$

$$CJV = \frac{\sigma(\mathrm{WM}) + \sigma(\mathrm{GM})}{|\,\mu(\mathrm{WM}) - \mu(\mathrm{GM})|} \tag{13}$$

where $\mu(x)$, $\sigma(x)$ are standard deviation and mean of tissue x. In order to demonstrate better efficiency, the CV and CJV value should be lowered.

By the avail of these datasets, three 3D models were formulated: (i) the ground truth model, (ii) the 3D model with bias correction and (iii) the 3D model without bias correction. The proposed algorithm is implemented by correcting bias and is represented by BC_3D (Bias Corrected 3D), while the 3D model formulated without bias correction is represented by BUC_3D. The following evaluation metrics are used to assess the performance of the Bias Corrected (BC_3D) and Bias UnCorrected 3D Model (BUC_3D): Volumetric Overlap Error (VOE), Relative Volume Difference (RVD), Average symmetric Surface Distance (ASD), Maximum symmetric Surface Distance (MSD), Accuracy (ACC), Sensitivity (SEN), Specificity (SPE), Precision (PRE), and FScore (FS).

Volumetric Overlap Error (VOE):

$$VOE = 1 - \frac{|\,A \cap B|}{|\,A \cup B|} \tag{14}$$

Relative Volume Difference (RVD):

$$RVD = \frac{|\,A| - |\,B|}{|\,B|} \times 100 \tag{15}$$

Average Symmetric surface Distance (ASD):

$$ASD = \frac{\sum_{x \in A} d(x, B) + \sum_{y \in B} d(y, A)}{|\,A| + |\,B|} \tag{16}$$

Maximum Symmetric surface Distance (MSD):

$$MSD = \max\left\{ d_H(A, B), d_H(B, A) \right\} \tag{17}$$

Accuracy (ACC):

$$ACC = \frac{TP + TN}{TP + TN + FP + FN} \tag{18}$$

Sensitivity or Recall (SEN):

$$SEN = \frac{TP}{TP + FN} \tag{19}$$

Specificity (SPE):

$$SPE = \frac{TN}{TN + FP} \tag{20}$$

Precision (PRE):

$$PRE = \frac{TP}{TP + FP} \tag{21}$$

F Score (FS):

$$FS = \frac{2 \times PRE \times SEN}{PRE + SEN} \tag{22}$$

where A represents segmented image volume and B represents the reference image volume, d is a distance, TP, TN, FP and FN denote True Positive, True Negative, False Positive and False Negative. In (17), $d_H(A,B)$ refers to the Hausdorff distance from set A to set B, where it measures how far the points of A are from B. To signify excellent performance, the values of Volumetric Overlap Error, Relative Volume Difference, Average Symmetric surface Distance, and Maximum Symmetric surface Distance should be low while Accuracy, Sensitivity, Specificity, Precision, and FScore values should be high.

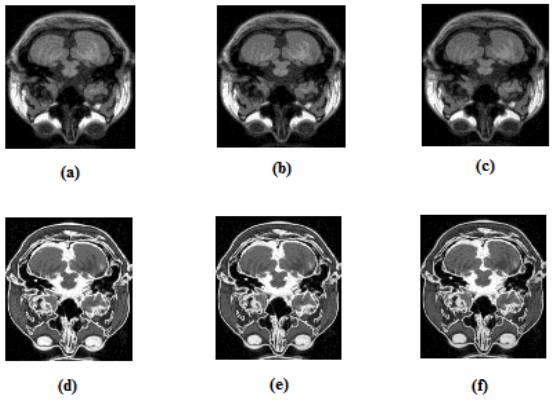

Fig.2. Input Images (a) T1 Weighted Images with zero percent Intensity Non-Uniformity (T1W 0% INU) (b) T1 Weighted images with twenty percent Intensity Non-Uniformity (T1W 20% INU) (c) T1 Weighted images with forty percent Intensity Non-Uniformity (T1W 40% INU) (d) T2 Weighted images with zero percent Intensity Non-Uniformity (T2W 0% INU) (e) T2 Weighted images with twenty percent Intensity Non-Uniformity (T2W 20% INU) (f) T2 Weighted images with forty percent Intensity Non-Uniformity (T2W 40% INU)

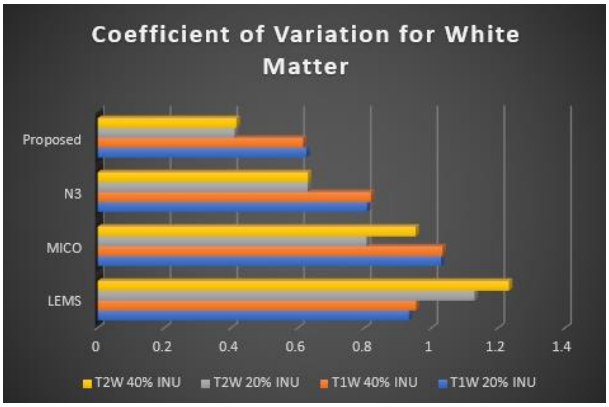

Fig.3. CV for white Matter for various bias correction algorithms (LEMS, MICO, N3 and Proposed) along with its bias input type (T1W 20% INU, T1W 40% INU, T2W 20% INU and T2W 40% INU)

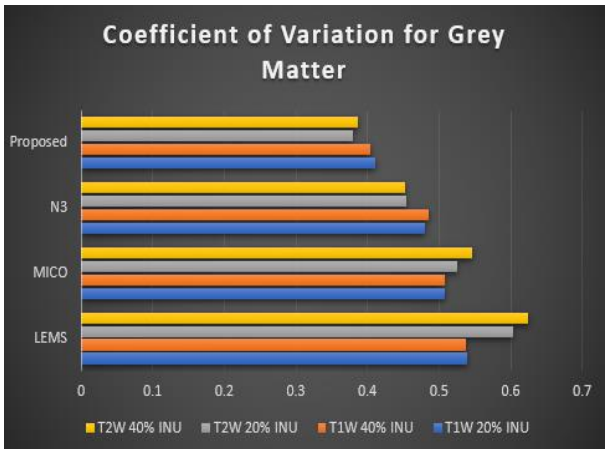

Fig.4. CV for Grey Matter for various bias correction algorithms (LEMS, MICO, N3 and Proposed) along with its bias input type (T1W 20% INU, T1W 40% INU, T2W 20% INU and T2W 40% INU)

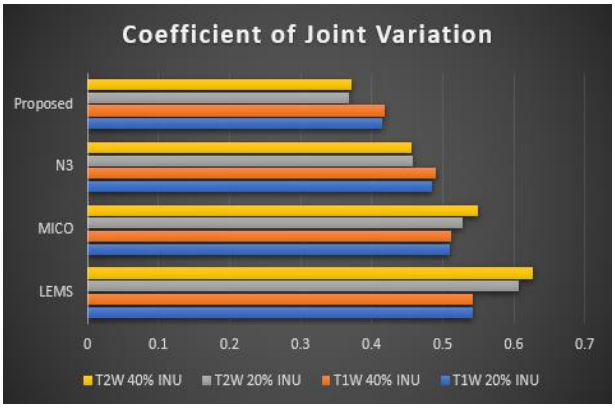

Fig.5. CJV for various bias correction algorithms (LEMS, MICO, N3 and Proposed) along with its bias input type (T1W 20% INU, T1W 40% INU, T2W 20% INU and T2W 40% INU)

The coefficients of variation (CV) for white matter for each bias correction algorithm are shown in Fig.3, along with the bias input data for each algorithm. The Fig.3 depicts that the proposed algorithm effectively removes bias fields, as evidenced by its lower white matter CV value of (± 0.5165), compared to the other algorithms: LEMS (± 1.0614), MICO (± 0.9544), and N3 (± 0.7210). The grey matter coefficients of variation (CV) for several bias correction techniques are shown in Fig.4, together with the bias input data for each algorithm. The Fig.4 confirms that the proposed algorithm outperforms the other algorithms as evidenced by its lower grey matter CV value of proposed (± 0.3947), compared to the other algorithms: LEMS (± 0.5760), MICO (± 0.5220), and N3 (± 0.4683). The Fig.5 reflects the Coefficient of Joint Variation (CJV), across different bias correction algorithms, along with their respective bias input data. proposed (± 0.3929), compared to the other algorithms: LEMS (± 0.5797), MICO (± 0.5249), and N3 (± 0.4720). The Fig.5 concludes that our proposed algorithm effectively removes non-perceptible bias when compared to state-of-the-art algorithms.

The Fig.6 lists the performance assessment of Volumetric Overlap Error (VOE), Relative Volume Difference (RVD), Average symmetric Surface Distance (ASD) and Maximum symmetric Surface Distance (MSD), for the formulated two 3D models (with and without bias correction) over the four types of input images (T1 weighted images with twenty percent Intensity Non-Uniformity, T1 weighted images with forty percent Intensity Non-Uniformity, T2 weighted images with twenty percent Intensity Non-Uniformity and T2 weighted images with forty percent Intensity Non-Uniformity). Fig.6 states that VOE, RVD, ASD and MSD values of BC_3D are lesser when compared with BUC_3D for all types of input categories.

The Fig.7 shows the performance assessment of ACC, SEN, SPE, PRE and FS for the constructed two 3D models (with and without bias correction) over the four types of input images (T1 weighted images with twenty percent Intensity Non-Uniformity, T1 weighted images with forty percent Intensity Non-Uniformity, T2 weighted images with twenty percent Intensity Non-Uniformity and T2 weighted images with forty percent Intensity Non-Uniformity). With the exception of T1W 20% INU

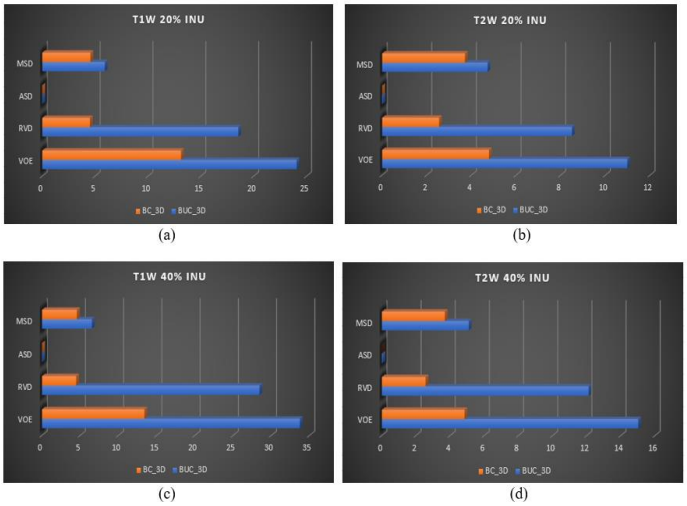

Fig.6. Performance assessment of VOE, RVD, ASD and MSD for two 3D models formulated (with bias correction (BC_3D) and without bias correction (BUC_3D)) over (a) T1 weighted images with 20 percentage Intensity Non-Uniformity, (b) T2 weighted images with 20 percentage Intensity Non-Uniformity, (c) T1 weighted images with 40 percentage Intensity Non-Uniformity, (d) T2 weighted images with 40 percentage Intensity Non-Uniformity sensitivity, the BC_3D model's

accuracy, sensitivity, specificity, precision, and FScore values are all greater than the BUC_3D for all input types.

T1W 20% INU's sensitivity for BUC_3D is 97.71606, while that of BC_3D is 97.52206. These values have a slight variance and fall within the same range. This also holds true for T2W 20% INU. Metrics like FScore, accuracy, and precision are prioritized over sensitivity and specificity. Thus, the overall conclusion drawn from Figures 6 and 7 is, compared to the model built without our suggested bias correction technique, the model built with it was more accurate in a quantitative sense.

Fig.8 depicts the axial view of the constructed 3D model: (a) represents the 3D model formulated from the slices of T1 weighted images with zero percent Intensity Non-Uniformity (ground truth image), (b) represents the 3D model formulated from the image slices of T1 weighted images with twenty percent Intensity Non-Uniformity (20% bias infused image) and (c) represents the 3D model formulated from the image slices of T1 weighted images with forty percent Intensity Non-Uniformity (40% bias infused image). No bias correction has performed at this state. This aims to demonstrate the impact of adding non-perceptible bias. From Fig.8, it clearly shown that the addition of bias causes the organ loss, it is visible in the area and size of brain region.

The Fig.9 depicts the axial view of formulated 3D model: (a) represents the 3D model formulated from the slices of T1 weighted images with zero percent Intensity Non-Uniformity (ground truth model), (b) represents the 3D model formulated from the T1 weighted images with twenty percent Intensity Non-Uniformity (BUC_3D) and (c) represents the 3D model

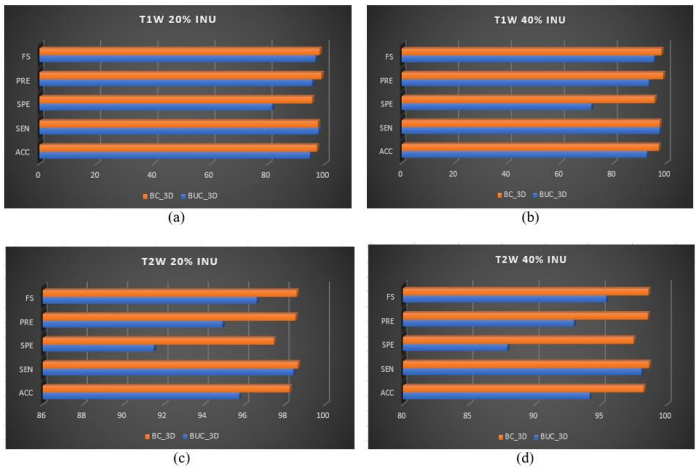

Fig.7. Performance assessment of VOE, RVD, ASD and MSD for two 3D models formulated (with bias correction (BC_3D) and without bias correction (BUC_3D)) over (a) T1 weighted images with 20 percentage Intensity Non-Uniformity, (b) T1 weighted images with 40 percentage Intensity Non-Uniformity (c) T2 weighted images with 20 percentage Intensity Non-Uniformity, (d) T2 weighted images with 40 percentage Intensity Non-Uniformity formulated from the outcome of our proposed algorithm for the image slices T1 weighted with twenty percent Intensity Non-Uniformity (BC_3D).

The 3D model from Fig.9(a) naturally consist of some gaps, but the 3D model formulated from the bias corrupted image in Fig.9(b) has the larger gaps in the skull area, but the bias corrected 3D model from Fig.9(c) retrains the original model, that is, our proposed method is able to remove the bias which leads to building the 3D model as the original one, so it can have the exact size of gaps as in the ground truth 3D model.

The Fig.10 shows the axial view of the formulated 3D model: (a) represents the 3D model formulated from the image slices of T2 weighted images with zero percent Intensity Non-Uniformity, (b) represents the 3D model formulated from the T2 weighted images with forty percent Intensity Non-Uniformity, and (c) represents the 3D model formulated from the outcome of our proposed algorithm for the image slices of T2 weighted with forty percent Intensity Non-Uniformity. By comparing the brain region from Fig.10(a), Fig.10(b) and Fig.10(c): the brain region was shrunk in bias corrupted 3D model, shown in Fig.10(b), but our proposed algorithm precisely builds the 3D model without the brain shrinkage, which is shown in Fig.10(c). The bias, which is hardly noticeable, still builds an erroneous 3D model with deprivation of organs. The proposed technique, which effectively removes the unnoticeable bias, accurately segments the image and precisely builds the 3D model. The quantitative metrics and qualitative assessment help in confirming the statement.

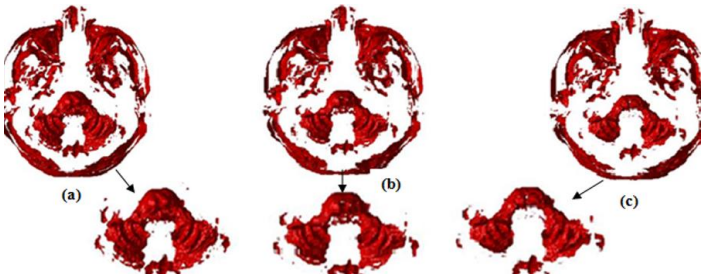

Fig.8. (a) 3D model of T1W with 0% INU, (b) 3D model of T1W with 20% INU, (c) 3D model of T1W with 40% INU

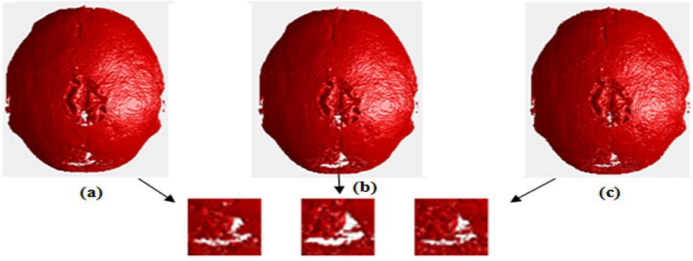

Fig.9. (a) 3D model of T1W with 0% INU, (b) 3D model of T1W with 20% INU without Bias Correction, (c) 3D model of T1W with 20% INU with Bias Correction

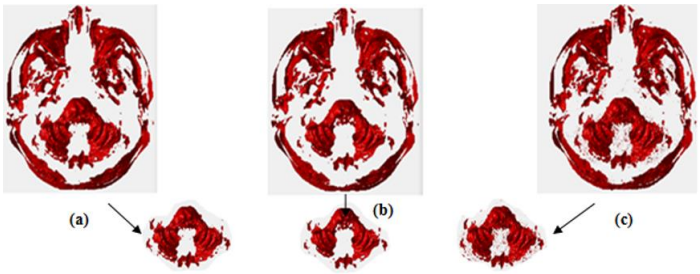

Fig.10. (a) 3D model of T2W with 0% INU, (b) 3D model of T2W with 40% INU without Bias Correction, (c) 3D model of T2W with 40% INU with Bias Correction

5. CONCLUSION

This paper proposed a novel technique that efficiently erodes the bias, which is hardly noticeable, and builds an accurate 3D model. The proposed algorithm incorporates gradient calculation, texture refinement, logarithmic transformation, ROI extraction, kernel construction, and bias correction operations in the pre-processing phase. The Distance Regularized Level Set Evaluation technique is used for segmenting the bias-corrected image, and the marching cube algorithm is used for 3D reconstruction. In terms of measuring the bias correction on 2D images, quantitative metrics, such as the Coefficient of Variation (CV) for white matter, grey matter, and Coefficient of Joint Variation (CJV), are used. The proposed technique outperforms the state-of-the-art algorithms LEMS, N3, and MICO by having lower CV and CJV values. To assess its performance in a more advanced manner, three types of 3D models were constructed: a 3D model with bias correction, a 3D model without bias correction, and a 3D model from ground truth images (i.e., a 3D model constructed from zero percent bias corrupted images). The metrics Volumetric Overlap Error (VOE), Relative Volume Difference (RVD), Average Symmetric surface Distance (ASD), Maximum Symmetric surface Distance (MSD), Accuracy (ACC), Sensitivity (SEN), Specificity (SPE), Precision (PREC), and F-Score (FS) are calculated on the constructed 3D models. To conclude the better performance, the VOE, RVD, ASD, and MSD values should be lower. ACC, SEN, SPE, PREC, and FS values should be higher. The outcome states that the bias-corrected 3D model of our proposed algorithm has higher ACC, SEN, SPE, PREC, and FS and lesser VOE, RVD, ASD, and MSD than the bias-uncorrected 3D model. By examining these three constructed 3D models, the bias uncorrected 3D model has some bigger holes and organ deterioration in size. And in the bias-corrected 3D model, all these shortcomings are negotiated, and it resembles the ground truth 3D model. The outcome concludes that the proposed algorithm efficiently corrects the lesser, unnoticeable bias and accurately constructs the error-free 3D model.

Further research efforts should be directed at improving the current bias correction technique through the application of deep learning and artificial intelligence approaches to achieve automatic estimation and correction of bias in medical images. The reliability of the presented technique should be tested using large numbers of medical imaging data sets that contain images of CT scans, PET scans, and multimodal MRI images. The real-time implementation of the suggested bias correction algorithm could help physicians with making clinical diagnoses and guiding surgery. The use of advanced segmentation algorithms can help detect boundaries between different tissues in complex anatomies more precisely. Adaptive construction of kernels can help handle different cases of inhomogeneities in the images' intensities. Cloud-based and parallel computation platforms can greatly increase the speed of 3D image reconstruction. Moreover, the suggested approach to bias correction can be applied to the analysis of images containing pathologies to help detect tumors.

REFERENCES

[1] U. Vovk, F. Pernujs and B. Likar, "A Review of Methods for Correction of Intensity Inhomogeneity in MRI", *IEEE Transactions on Medical Imaging*, Vol. 26, No. 3, pp. 405-421, 2007.

[2] Z. Hou, "A Review on MR Image Intensity Inhomogeneity Correction", *International Journal of Biomedical Imaging*, Vol. 2006, No. 1, pp. 1-11, 2006.

[3] M.A. Balafar, A.R. Ramli, M.I. Saripan and S. Mashohor, "Review of Brain MRI Image Segmentation Methods", *Journal of Artificial Intelligence*, Vol. 33, pp. 261-274, 2010.

[4] B. Belaroussia, J. Millesb, S. Carmec, Y.M. Zhua and H. Benoit-Cattin, "Intensity Nonuniformity Correction in MRI: Existing Methods and their Validation", *Medical Image Analysis*, Vol. 10, pp. 234-246, 2006.

[5] G.H. Glover, C.E. Hayes and N.J. Pelc, "Comparison of Linear and Circular Polarization for Magnetic Resonance Imaging", *Journal of Magnetic Resonance*, Vol. 64, No. 2, pp. 255-270, 1985.

[6] I. Harvey, P.S. Tofts, J.K. Morris, D.A.G. Wicks and M.A. Ron, "Sources of T1 Variance in Normal Human White Matter", *Magnetic Resonance Imaging*, Vol. 9, No. 1, pp. 53-59, 1991.

[7] A. Simmons, P.S. Tofts, G.J. Barker and S.R. Arridge, "Sources of Intensity Nonuniformity in Spin Echo Images at 1.5T", *Magnetic Resonance in Medicine*, Vol. 32, No. 1, pp. 121-128, 1994.

[8] G.J. Barker, A. Simmons, S.R. Arridge and P.S. Tofts, "A Simple Method for Investigating the Effects of Non-Uniformity of Radiofrequency Transmission and Radiofrequency Reception in MRI", *British Journal of Radiology*, Vol. 71, No. 841, pp. 9-67, 1998.

[9] M. Alecci, C.M. Collins, M.B. Smith and P. Jezzard, "Radio Frequency Magnetic Field Mapping of a 3 Tesla Birdcage Coil", *Magnetic Resonance in Medicine*, Vol. 46, No. 2, pp. 379-385, 2001.

[10] M. Ganzetti, N. Wenderoth and D. Mantini, "Quantitative Evaluation of Intensity Inhomogeneity Correction Methods for Structural MR Brain Images", *Neuroinformatics*, Vol. 14, No. 1, pp. 5-21, 2015.

[11] Z.P. Liang and P.C. Lauterbur, "*Principles of Magnetic Resonance Imaging: A Signal Processing Perspective*", 2000.

[12] E.R. McVeigh, M.J. Bronskill and R.M. Henkelman, "Phase and Sensitivity of Receiver Coils in Magnetic Resonance Imaging", *Medical Physics*, Vol. 13, pp. 806-814, 1986.

[13] L. Axel, J. Costantini and J. Listerud, "Technical Note Intensity", *American Journal of Roentgenology*, Vol. 148, pp. 418-420, 1987.

[14] D.A.G. Wicks, G.J. Barker and P.S. Tofts, "Correction of Intensity Nonuniformity in MR Images of any Orientation", *Magnetic Resonance Imaging*, Vol. 11, pp. 183-196, 1993.

[15] Z. Hou, "A Review on MR Image Intensity Inhomogeneity Correction", *International Journal of Biomedical Imaging*, pp. 1-11, 2006.

[16] U. Vovk, F. Pernus and B. Likar, "A Review of Methods for Correction of Intensity Inhomogeneity in MRI", *IEEE Transactions on Medical Imaging*, Vol. 26, No. 3, pp. 1-7, 2007.

[17] H. Liu, "Original Intensity Preserved Inhomogeneity Correction and Segmentation for Liver Magnetic Resonance

Imaging", *Biomedical Signal Processing and Control*, Vol. 47, pp. 231-239, 2019.

[18] N. Mahata, "Local Contextual Information and Gaussian Function Induced Fuzzy Clustering Algorithm", *Applied Soft Computing*, Vol. 68, pp. 586-596, 2018.

[19] P. Mishro, "Novel Fuzzy Clustering-based Bias Field Correction Technique for Brain Magnetic Resonance Images", *IET Image Processing*, Vol. 14, pp. 1-11, 2020.

[20] M.N. Ahmed, "A Modified Fuzzy C-Means Algorithm for Bias Field Estimation and Segmentation of MRI Data", *IEEE Transactions on Medical Imaging*, Vol. 21, pp. 193-199, 2002.

[21] A.W. Liew and H. Yan, "An Adaptive Spatial Fuzzy Clustering Algorithm for 3-D MR Image Segmentation", *IEEE Transactions on Medical Imaging*, Vol. 22, pp. 1063-1075, 2003.

[22] K.S. Chuang, "Fuzzy C-Means Clustering with Spatial Information for Image Segmentation", *Computerized Medical Imaging and Graphics*, Vol. 30, pp. 9-15, 2006.

[23] W. Cai, S. Chen and D. Zhang, "Fast and Robust Fuzzy C-Means Clustering Algorithms Incorporating Local Information for Image Segmentation", *Pattern Recognition*, Vol. 40, pp. 835-838, 2007.

[24] Z. Wang, "An Adaptive Spatial Information-Theoretic Fuzzy Clustering Algorithm for Image Segmentation", *Computer Vision and Image Understanding*, Vol. 117, pp. 1412-1420, 2013.

[25] A.N. Benaichouche, "Improved Spatial Fuzzy C-Means Clustering for Image Segmentation", *Digital Signal Processing*, Vol. 23, pp. 390-1400, 2013.

[26] C. Li, "MRI Tissue Classification and Bias Field Estimation based on Coherent Local Intensity Clustering", *Proceedings of International Conference on Information Processing in Medical Imaging*, pp. 288-299, 2009.

[27] Z.X. Ji, "A Modified Possibilistic Fuzzy C-Means Clustering Algorithm for Bias Field Estimation", *Computerized Medical Imaging and Graphics*, Vol. 35, No. 5, pp. 383-397, 2011.

[28] M. Xie, "A Modified Method for MRF Segmentation and Bias Correction of MR Image with Intensity Inhomogeneity", *Medical and Biological Engineering and Computing*, Vol. 53, No. 1, pp. 23-35, 2015.

[29] C. Li, J.C. Gore and C. Davatzikosa, "Multiplicative Intrinsic Component Optimization (MICO) for MRI Bias Field Estimation and Tissue Segmentation", *Magnetic Resonance Imaging*, Vol. 32, pp. 913-923, 2014.

[30] M.N. Ahmed, "A Modified Fuzzy C-Means Algorithm for Bias Field Estimation and Segmentation of MRI Data", *IEEE Transactions on Medical Imaging*, Vol. 21, No. 3, pp. 1-9, 2002.

[31] K. Zhang, "A Variational Approach to Simultaneous Image Segmentation and Bias Correction", *IEEE Transactions on Cybernetics*, Vol. 45, No. 8, pp. 1426-1437, 2015.

[32] C. Li, "A Variational Level Set Approach to Segmentation and Bias Correction of Images with Intensity Inhomogeneity", *Proceedings of International Conference on Medical Image Computing and Computer-Assisted Intervention*, pp. 1083-1091, 2008.

[33] L. Wang and C. Pan, "Image-Guided Regularization Level Set Evolution for MR Image Segmentation and Bias Field Correction", *Magnetic Resonance Imaging*, Vol. 32, No. 1, pp. 71-83, 2014.

[34] Y. Duan, "The L0 Regularized Mumford-Shah Model for Bias Correction and Segmentation of Medical Images", *IEEE Transactions on Image Processing*, Vol. 24, No. 11, pp. 3927-3938, 2015.

[35] R. Gonzalez and R. Woods, "*Digital Image Processing*", 2002.

[36] D.L. Pham and J.L. Prince, "An Adaptive Fuzzy C-Means Algorithm for Image Segmentation in the Presence of Intensity Inhomogeneities", *Pattern Recognition Letters*, Vol. 20, No. 1, pp. 57-68, 1999.

[37] C. Li, "A Level Set Method for Image Segmentation in the Presence of Intensity Inhomogeneities with Application to MRI", *IEEE Transactions on Image Processing*, Vol. 20, pp. 2007-2016, 2011.

[38] M. Singh, "Enhancement and Intensity Inhomogeneity Correction of Diffusion-Weighted MR Images", *Journal of Medical and Biological Engineering*, Vol. 37, pp. 508-518, 2017.

[39] V.S. Nguyen, M.H. Tran and H.M. Quang Vu, "A Research on 3D Model Construction from 2D DICOM", *Proceedings of International Conference on Advanced Computing and Applications*, pp. 158-163, 2016.

[40] Z. Pan, "Comparison of Medical Image 3D Reconstruction Rendering Methods for Robot-Assisted Surgery", *Proceedings of International Conference on Advanced Robotics and Mechatronics*, pp. 94-99, 2017.

[41] Y.T. Chen, "A Novel Approach to Segmentation and Measurement of Medical Image using Level Set Methods", *Magnetic Resonance Imaging*, Vol. 39, pp. 175-193, 2017.

[42] A. Kalra, "Developing FE Human Models from Medical Images", *Basic Finite Element Method as Applied to Injury Biomechanics*, pp. 389-415, 2018.

[43] B. Hou, "3-D Reconstruction in Canonical Co-Ordinate Space from Arbitrarily Oriented 2-D Images", *IEEE Transactions on Medical Imaging*, Vol. 37, No. 8, pp. 1737-1750, 2018.

[44] M. Al-Ayyoub, "Accelerating 3D Medical Volume Segmentation using GPUs", *Multimedia Tools and Applications*, Vol. 77, pp. 4939-4958, 2018.

[45] I. Mehmood, "An Efficient Computerized Decision Support System for the Analysis and 3D Visualization of Brain Tumor", *Multimedia Tools and Applications*, Vol. 78, pp. 12723-12748, 2019.

[46] P. Visutsak, "Marching Cubes and Histogram Pyramids for 3D Medical Visualization", *Journal of Imaging*, Vol. 6, No. 9, pp. 1-12, 2020.

[47] A. Farzana, M. Mohamed Sathik and S. Shajun Nisha, "Performance Analysis of Bias Correction Techniques in Brain MR Images", *International Journal of Information Technology*, Vol. 12, pp. 899-905, 2020.

[48] A. Farzana, M. Mohamed Sathik and S. Shajun Nisha, "Factual Foreground Segregation and Gradient based Bias Correction in Brain MR Images", *Journal of Mathematical and Computational Science*, Vol. 11, pp. 3037-3051, 2021.

[49] C. Li, "Distance Regularized Level Set Evolution and its Application to Image Segmentation", *IEEE Transactions on Image Processing*, Vol. 19, No. 12, pp. 3243-3254, 2010.

[50] W.E. Lorensen and H.E. Cline, "Marching Cubes: A High Resolution 3D Surface Construction Algorithm", *ACM SIGGRAPH Computer Graphics*, Vol. 21, No. 4, pp. 163-169, 1987.

[51] C.A. Cocosco, "BrainWeb: Online Interface to a 3D MRI Simulated Brain Database", *NeuroImage*, Vol. 5, No. 4, pp. 1-4, 1997.

[52] O. Salvado, "Method to Correct Intensity Inhomogeneity in MR Images for Atherosclerosis Characterization", *IEEE Transactions on Medical Imaging*, Vol. 25, No. 5, pp. 539-552, 2006.

[53] O. Salvado, "Intensity Inhomogeneity Correction", Available at: https://www.mathworks.com/matlabcentral/fileexchange/13411-intensity-inhomogeneity-correction, Accessed in 2020.

[54] C. Li, J.C. Gore and C. Davatzikosa, "Multiplicative Intrinsic Component Optimization (MICO) for MRI Bias Field Estimation and Tissue Segmentation", *Magnetic Resonance Imaging*, Vol. 32, pp. 913-923, 2014.

[55] J.G. Sled, A.P. Zijdenbos and A.C. Evans, "A Nonparametric Method for Automatic Correction of Intensity Nonuniformity in MRI Data", *IEEE Transactions on Medical Imaging*, Vol. 17, No. 1, pp. 87-97, 1998.